Astron. Astrophys. 260, 397–410 (1992)

ASTRONOMY AND ASTROPHYSICS

Long-slit spectroscopy of the planetary nebula NGC 6543: collimated bipolar ejections from a precessing central source?

L. F. Miranda and J. Solf

Max-Planck-Institut für Astronomie, Königstuhl 17, D-6900 Heidelberg 1, Germany

Received November 6, 1991; accepted February 1, 1992

Abstract. Long-slit spectra of the planetary nebula NGC 6543, obtained at high and moderate spectral and high spatial resolution, are presented. The data allow us to study the spatial and kinematical properties of the various components identified in the nebula in great detail and to establish a spatio-kinematical model which can account for the observed velocity field. The basic structure of the nebula is a geometrically thick expanding ellipsoid, mainly defined by an inner shell and an outer shell. A bright ring defines the equatorial plane of the thick ellipsoid. The equatorial expansion velocity in the thick ellipsoid varies from $\approx 16\,\mathrm{km\,s^{-1}}$, at its inner shell, up to $\approx 28\,\mathrm{km\,s^{-1}}$, at its outer shell. The polar expansion velocities exceed the equatorial velocities by a factor of ≈ 1.8. Four pairs of narrow, point-symmetric components have been identified in the object, including the previously known bipolar jet-like features. Each pair of point-symmetric components exhibits a filamentary structure characterized by systematic variations of the position and radial velocity. Three of the pairs are embedded in the outer shell of the thick ellipsoid and participate in its expansion. The fourth pair (the bipolar jet-like features) is neither geometrically nor kinematically related to the thick ellipsoid; it seems to be younger than the other nebular components and to move at a higher velocity. The peculiar spatial and kinematical structure deduced for the point-symmetric components, particularly for the jet-like features, is probably the result of highly collimated bipolar mass ejections from the central star. Moreover, the structure suggests that the ejections have occurred along a precessing bipolar axis and that the precession parameters have changed with time.

The observed line ratios suggest that shock excitation seems to exist in some of the point-symmetric components and in the jet-like features. The electron density and estimates of the ionized mass have been derived for the prominent components. Minimum values of the electron density ($\approx 10^3\,\mathrm{cm^{-3}}$) and ionized mass ($\approx 2.5\ 10^{-4}\,M_\odot$) are found in the jet-like features.

The results favor the proposition that the central object of NGC 6543 is a binary. In this model, the thick ellipsoid results from the interaction of an energetic stellar wind with material of a circumbinary envelope (dispersed during the AGB phase of the primary) which presents an anisotropic density distribution. The filamentary, point-symmetric components are attributed to highly collimated bipolar ejections from the inner parts of an accretion disk about the compact companion. The particular shape of the ejected components can be explained by precession of that disk.

Send offprint requests to: J. Solf

Key words: planetary nebulae: individual: NGC 6543 – interstellar medium: jets and outflows – interstellar medium: kinematics and dynamics – stars: mass loss

1. Introduction

According to the interacting stellar winds (ISW) model for the formation of planetary nebulae (PNs) (Kahn 1989 and Kwok 1989, and references therein), the "PN system" (Kwok 1989) consists of a central star, an energetic stellar wind, an expanding ionized shell, and the remnant envelope of the progenitor red giant. The observations show that most PNs can basically be described in terms of ISW (e.g. Balick 1987 and Soker & Livio 1989, and references therein). However, the model finds some difficulties to explain polar condensations (often observed in bipolar PNs), bipolar jets detected in some PNs, and complex PNs with multiple shell components (Gieseking et al. 1985; Balick & Preston 1987, see below; Soker 1990; Solf & Miranda 1992; Icke et al. 1991). In these cases, peculiar ejection processes, related to the evolution and/or the nature of the central star, have been invoked (Morris 1987; see references above).

NGC 6543, one of the most complex PNs known, displays the peculiar characteristics mentioned above. On direct images (Fig. 1; see also Münch 1968; Bignell 1983; Balick & Preston 1987, hereafter BP), the appearance of the object is rather unusual for PNs. In the light of the Hα and [O III] lines, two bright "ellipses" are observed, each of them centered on the central star, whose major axes are perpendicular to each other and oriented at position angle (PA) $\approx 25°$ and $\approx 115°$, respectively. The two ellipses, hereafter referenced as the "PA 25° Ellipse" and the "PA 115° Ellipse" (see Fig. 1), can also be seen on VLA maps at 6 cm and 20 cm (Bignell 1983; Balick et al. 1987a, hereafter BBHO). Remarkably, the PA 25° Ellipse is not present on direct images obtained in the light of low excitation lines ([N II], [O I], [S II]). On the other hand, those images show two prominent polar caps (Fig. 1) that are not detected on [O III] maps of NGC 6543. All these structures are closely surrounded by a fainter elliptical envelope which presents a rather steep intensity gradient (Phillips et al. 1979; BP; see also Fig. 1). Along the major axis of the elliptical envelope (oriented at PA $\approx 25°$) and beyond the polar caps, two bright polar condensations (Fig. 1) are observed which are particularly prominent in the low-excitation lines. In addition, two bipolar jet-like features (BP: "tails"; Miranda & Solf 1990)

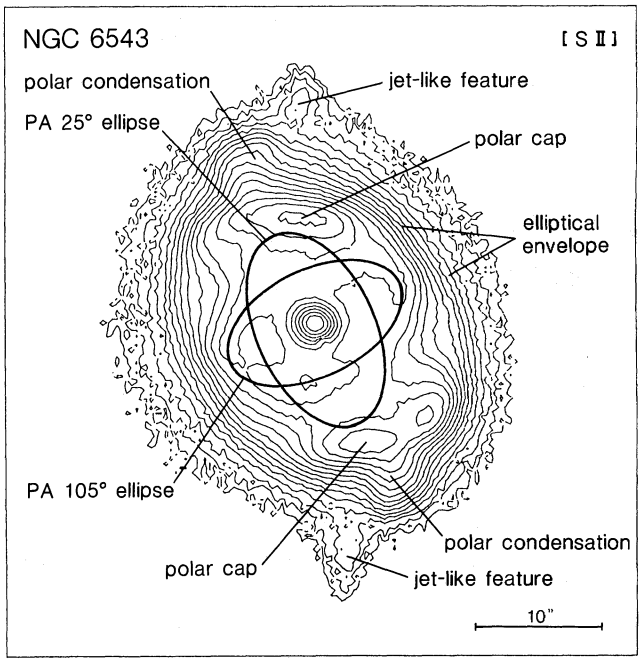

Fig. 1. Isocontour map of NGC 6543 in the light of the [S II] 6716+6731 lines deduced from a narrow-band direct CCD image. The contour spacing is logarithmic, corresponding to a factor $2^{1/2}$ in intensity. North is up, east to the left. The nebular components (see text) are marked

have been detected in NGC 6543 near the north-south direction, outside the elliptical envelope. The outermost regions of the jet-like features can be seen on direct images (Fig. 1) where they appear slightly curved (BP). However, the features can be traced more inside the nebula as well (Miranda & Solf 1990). Intriguingly, the jet-like features are not oriented along the major axis of the elliptical envelope (see above). Nevertheless, the whole nebular complex (including the jet-like features) exhibits a remarkable point symmetry with respect to the central star. The bright regions of NGC 6543 (just described) are surrounded by a faint spherical, knotty halo of $\approx 5'$ in diameter (Millikan 1974; see also Pottasch 1984).

The physical conditions within NGC 6543 also seem to be peculiar. In spite of remarkable similarities in their morphology, the PA 25° Ellipse and the PA 115° Ellipse present very different physical conditions (see above). The strong low-excitation line emission observed in the polar caps and the bipolar condensations suggests the existence of shock excitation and/or peculiar abundances in these components (BBHO). From the [S II] emission lines, Boeshaar et al. (1974) deduced electron densities of $\approx 4\ 10^4\,\mathrm{cm}^{-3}$ in the polar caps. In addition, these authors reported on density and temperature fluctuations within the nebula. The bipolar jet-like features are particularly prominent in the low-excitation lines (BBHO; Miranda & Solf 1990), although their excitation conditions have not been studied in detail.

Münch (1968) showed that the velocity field in NGC 6543, derived from multi-slit observations of the [O III] emission lines, is extremely complex. He proposed a spheroidal model for the nebula with the material located mainly on the surface of two helical structures. Phillips et al. (1979), using electronographic images of NGC 6543 and the velocity field from Münch, suggested that the nebula has the form of a three-axial ellipsoid. More recently, BP proposed a model consisting of two pairs of expanding bipolar lobes, oriented such that the two bipolar axes are perpendicular to each other, in order to account for the formation of the nebula in the context of the ISW model. Their hypothesis was based on the appearance of NGC 6543 at optical and radio wavelengths, but seems to be difficult to be reconciled with the kinematical data. In particular, BP pointed out that the polar caps and the tails (jet-like features) are not well incorporated in their model and suggested collimated mass ejections from the central star, along a precessing axis, in order to account for the curvature of the tails (see above). All these results show that several questions, regarding the basic geometric and kinematic structure of NGC 6543, are still not well answered. It seems that a single-component model can not account for the complex velocity field. If so, how many components do exist in the object? Which are the relationships between the components, if any? Can the formation of the entire object be explained by the ISW model?

In order to answer these questions, a detailed knowledge of the kinematics of the nebula is of crucial importance. In this paper, we present long-slit spectroscopic observations of NGC 6543. The new spectra have higher spectral and spatial resolution than previous ones, and permit a clear distinction of the various components existing in the object and to study their spatial and kinematical properties in great detail. In addition, the spectra allow us to estimate the excitation conditions within the various components. Combining all the information available from the spectra, we attempt to establish a spatio-kinematical model for NGC 6543, which can account for the complex velocity field. Moreover, the results allow us to impose constraints on the process of formation of the nebula.

2. Observations

The observations were carried out using the coudé spectrograph of the 2.2 m telescope and the Cassegrain twin spectrograph of the 3.5 m telescope, at the Calar Alto Observatory. In the case of the coudé spectrograph, we used the *f*/3 camera (90 cm focal length) and the *f*/12 camera (360 cm focal length), and as detectors either a GEC CCD with 396 × 576 pixels of 22 μm or a two-stage image intensifier tube, cooled at −18°C. The reciprocal linear dispersions are $2.2\,\text{Å}\,\mathrm{mm}^{-1}$ for the *f*/12 CCD spectra, $7.6\,\text{Å}\,\mathrm{mm}^{-1}$ for the *f*/3 image tube spectra, and $1.8\,\text{Å}\,\mathrm{mm}^{-1}$ for the *f*/12 image tube spectra. The image tube spectra were recorded on IIa-O plates pressed onto the fiber optics exit window of the tube. These spectrograms were digitized on a PDS microdensitometer. In the case of the Cassegrain spectrograph, a RCA CCD with 640 × 1024 pixels of 15 μm was used as detector in the red channel of the spectrograph. The dispersion is $36\,\text{Å}\,\mathrm{mm}^{-1}$. Because of the remarkable point-symmetry of the nebula with respect to the central star, the slits of the spectrographs were always centered on the central star and set to various PAs. Figure 1 shows an isocontour map of NGC 6543 derived from a CCD image (kindly provided by Dr. Hopp) in the light of the [S II] 6716+6731 emission lines. The used slit positions are indicated in Fig. 2. The Journal of the observations is summarized in Table 1. The data reduction procedures have been described elsewhere (Solf & Carsenty 1982).

3. Results

3.1. General properties of the emission lines

Figure 3a presents an enlargement of a high-resolution long-slit image tube spectrogram (L 3051, see Table 1) of the [N II] 6583 line

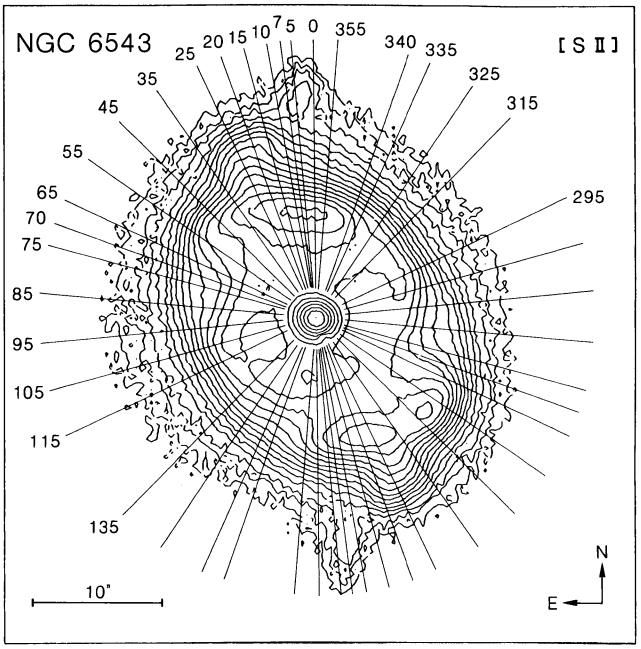

Fig. 2. Same as Fig. 1. The used spectrograph slit positions are indicated

obtained at PA 7°. The same line is shown in Fig. 3b as a (logarithmic) isophotic contour map in a position-velocity (PV) representation. (It should be noted that PA 7° corresponds to the "PA 2°" erroneously quoted by Miranda & Solf 1990.) The [N II] emission has been resolved into a large number of components which can be distinguished by both their spectral and spatial attributes, and by their internal intensity distribution. In particular, one recognizes an inner elliptical feature, surrounded by various components with a rather "compact" appearance in the spatial (direction of the slit) and velocity (direction of the dispersion) coordinates, and two rather elongated (direction of the slit), narrow (direction of the dispersion) components.

As one can immediately see in Fig. 3a, b, the [N II] emission line feature exhibits an exceedingly high point-symmetry with respect to the center. In particular, the upper half (direction of the slit) of the emission feature appears as the mirror image (wavelength direction reversed) of the lower half. For (almost) each component identified in the upper half of the emission feature, one can find a counterpart in the lower half, such that each component and its counterpart are located symmetrically with respect to both the position of the central star and the velocity centroid of the [N II] emission feature. In the following, the components detected in the northern half of the nebula will be denoted by A, B, C, D and J, their corresponding counterparts by A′, B′, C′, D′ and J′ (Fig. 3b).

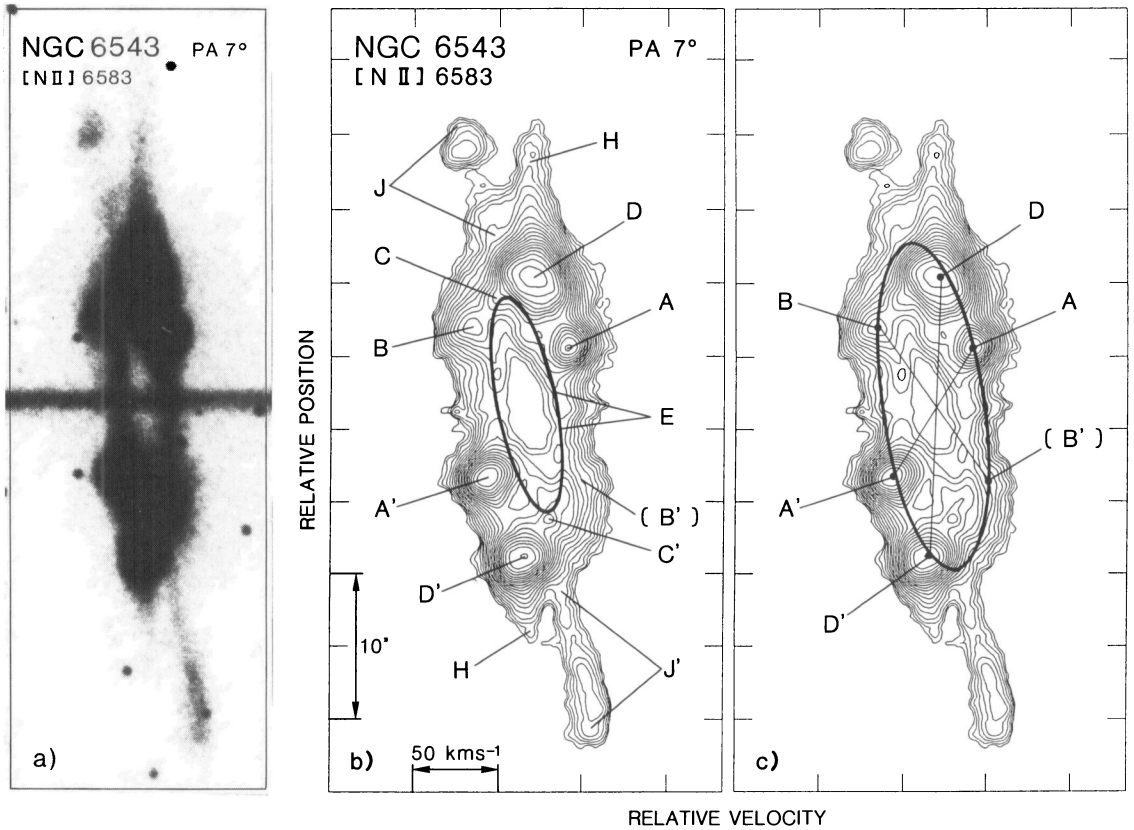

Fig. 3. **a** Enlarged high-resolution long-slit spectrogram of NGC 6543 obtained at PA 7° showing the [N II] 6583 line. The original dispersion is 1.8 Å mm^{-1}. **b** Position-velocity map of the line feature shown in the left-hand panel. The stellar continuum has been subtracted. The contour spacing is logarithmic, corresponding to a factor $2^{1/2}$ in intensity. The line feature is resolved into a large number of components which are arranged in a point symmetric pattern with respect to the center. For each component in the northern half of the line feature, a counterpart can be found in the southern half. Components in the northern half are denoted by A, B, C, D and J, their counterparts in the southern half by A′, B′, C′, D′ and J′. The central elliptical feature E (see text) is marked (continuous line). **c** Same as in the center panel. The intensity peaks of the two components of each pair are connected by a straight line. All lines virtually intersect in a single point which coincides with the centroid of the entire line feature. The centroid of the line feature coincides with the stellar position and represents the systemic radial velocity $V_{\odot} = -63.5$ km s^{-1}. The intensity peaks of these components (except JJ′) trace an outer ellipse, as indicated

Table 1. Journal of observations

Plate number	Date	Position angle (degree)	Spectral resolution (FWHM) ($km\,s^{-1}$)	Seeing (arcsec)	Exposure time (s)	Spectral range (Å)
L746	26-6-82	340	6	3	1800	6530–6600
L748	26-6-82	70	5	3	600	6530–6600
L749	26-6-82	25	5	3	600	6530–6600
L750	26-6-82	295	5	3	600	6530–6600
L2122	23-6-85	20	10	2	1800	6560–6590
L2146	24-6-85	20	13	3	1200	9060–9080
L3026	20-9-86	5	6	1	900	6530–6600
L3027	20-9-86	15	6	1	900	6530–6600
L3028	20-9-86	25	6	1	900	6530–6600
L3029	20-9-86	35	6	1	900	6530–6600
L3030	20-9-86	45	6	1	900	6530–6600
L3031	20-9-86	55	6	1	900	6530–6600
L3032	20-9-86	355	6	1	1020	6530–6600
L3033	20-9-86	0	6	1	900	6530–6600
L3034	20-9-86	10	6	1	900	6530–6600
L3035	20-9-86	315	6	1	900	6530–6600
L3036	20-9-86	325	6	1.5	900	6530–6600
L3037	20-9-86	85	6	1.5	900	6530–6600
L3038	20-9-86	95	6	1.5	900	6530–6600
L3039	20-9-86	105	6	1.5	900	6530–6600
L3042	20-9-86	65	6	1.5	900	6530–6600
L3043	20-9-86	335	6	1.5	900	6530–6600
L3051	21-9-86	7	6	0.7	3600	6530–6600
S 3087	23-9-86	7	10	1	600	6460–6770
L3101	24-9-86	7	10	3	3600	5002–5022
L3103	24-9-86	55	10	3	1200	5002–5022
L3105	24-9-86	75	10	3	1200	5002–5022
L3106	24-9-86	95	10	3	1200	5002–5022
L3107	24-9-86	115	10	3	1200	5002–5022
L3108	24-9-86	135	10	3	1200	5002–5022
L3124	25-9-86	295	10	1.5	1200	5002–5022
L3125	25-9-86	340	10	1.5	1200	5002–5022
L3126	25-9-86	25	10	1.5	1200	5002–5022
L3127	25-9-86	70	10	1	1200	5002–5022
T0168	02-6-88	5	47	1	300	6245–6755
T0171	02-6-88	5	54	1.5	1800	6245–6755

Each pair of components AA′ to JJ′ will be referred to as "pair of symmetric components". The inner elliptical line feature (marked in Fig. 3b) will be denoted by E. In addition, weak extended line emission (component H in Fig. 3b) has been detected at a radial velocity which coincides with the centroid radial velocity of the [N II] emission feature. This weak emission probably arises from the innermost regions of the extended halo around the nebula.

We note that the intensity peaks of components AA′, B and DD′ trace an outer ellipse on the PV map, as it is illustrated in Fig. 3c. Moreover, if the intensity peaks of each pair of symmetric components are connected by a straight line, all lines practically intersect in a single point which is located very close to the stellar position and at a radial velocity $V_{\odot} = -63.5\,km\,s^{-1}$ ($V_{LSR} = -47.5\,km\,s^{-1}$) (see Fig. 3c). In the following, we will adopt $-63.5\,km\,s^{-1}$ as the systemic velocity of the nebula. It agrees with the value obtained by other authors (see Schneider et al. 1983 and references therein). Radial velocities of internal motions within the nebula will be quoted thereafter with respect to the systemic velocity.

Figure 4 presents the PV maps of the [N II] 6583 emission line for 12 different PAs, deduced from the *f*/12 image tube spectra. These maps strengthen the results above mentioned. In particular, pairs of symmetric components are observed at almost every PA. In addition, the intersection point of lines connecting the intensity peaks of pairs of symmetric components (see above) always coincides with the centroid of the [N II] emission feature. As it can be seen in Fig. 4, the structure of the [N II] emission feature does not change much in small PA intervals of typically $\approx 20°$. This result, and the high number of closely spaced slit positions (Fig. 2), allow us to recognize each component, identified in Fig. 3b, at other PAs as well. In addition, we can identify an additional pair of symmetric components (at PAs around 25°) denoted by FF′. It can be recognized in Fig. 4 that only components AA′ and the inner ellipse E are present at all PAs. The other components (BB′

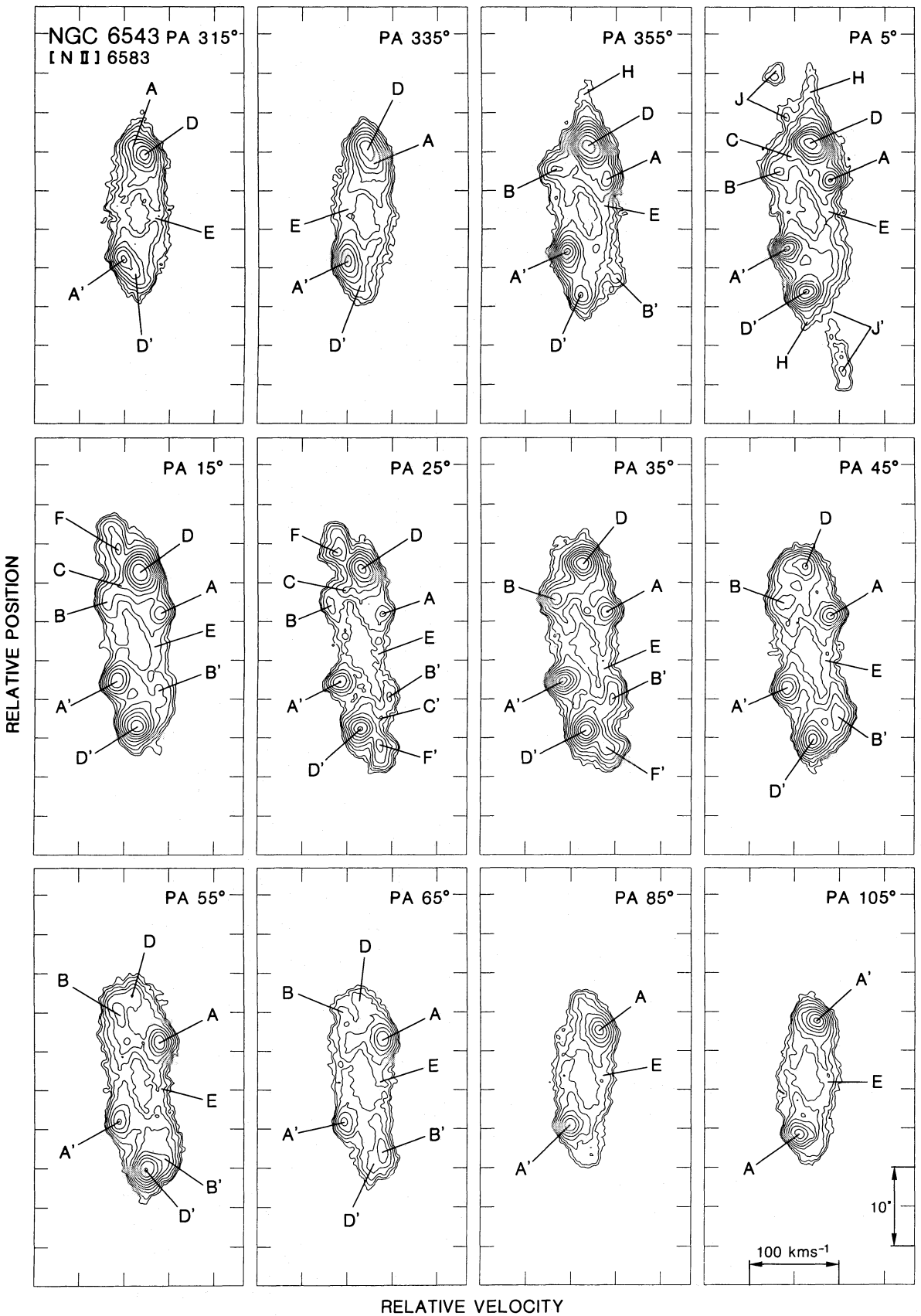

Fig. 4. High-resolution position-velocity maps of the [N II] 6583 emission line obtained at various PAs (indicated in the upper right of each panel). The contour spacing is logarithmic, corresponding to a factor 2 in intensity. The identified line components are indicated

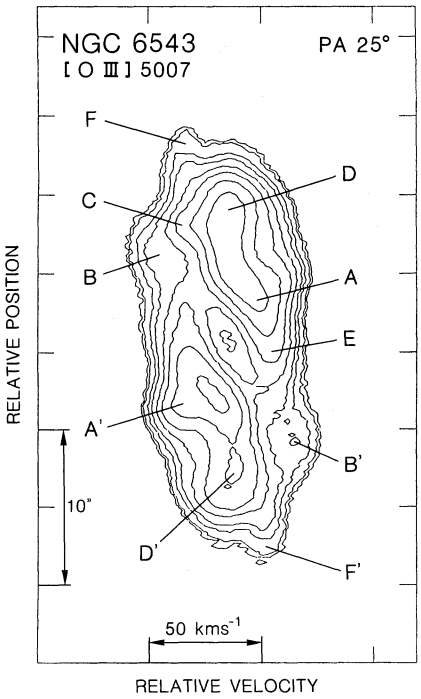

Fig. 5. High-resolution position-velocity map of the [O III] 5007 emission line obtained at PA 25°. The contour spacing corresponds to a factor $2^{1/2}$ in intensity. The identified line components are indicated

to JJ′) are observed in limited intervals of PAs only. Figure 4 further suggests that the line emission of components AA′ to FF′ arises in regions that are characterized by a small angular extent in the radial direction (along the slit) and a low velocity dispersion. Furthermore, on each PV map, the intensity peaks of AA′, BB′, DD′ and FF′ trace an outer ellipse. This ellipse is tilted (with respect to a vertical line on the PV maps); the tilt and size of the ellipse vary with the PA. Maximum tilt and maximum size of the ellipse are observed at PA 25°.

Figure 5 presents a PV map of the (high-excitation) [O III] 5007 emission line at PA 25°, deduced from a *f*/12 CCD spectrum (L 3116, see Table 1). Remarkably, in spite of the different spectral and spatial resolutions, all components observed in the [N II] emission (Fig. 4) can be identified in the [O III] emission line as well. This is also true for the observed Hα, He I, [O I], [S II] and [S III] emission lines (not shown). We note that the relative intensities of the various components are different for the different emission lines, suggesting that the physical conditions in the nebular components may also be different. This finding corresponds to the fact that the appearance of NGC 6543 on narrow-band images is different for different emission lines (see Introduction).

3.2. Spatio-kinematic properties of the various nebular components

Since the PV maps of the various emission lines show the same components, we can restrict our analysis of the kinematical and spatial properties of the components to the [N II] 6583 emission line which has been observed at higher resolution. In a first step, we deduced the radial velocity field for each component, using the intensity peak of the corresponding line feature as indicator of the radial velocity. Figure 6 shows the radial velocity distribution for each individual pair of symmetric components, superimposed on the [S II] image of NGC 6543. (The inner ellipse E and the components CC′, not shown in Fig. 6, will be described later).

In a second step, the velocity width and angular width (FWHM) were determined for each component of the [N II] emission on the contour maps (Figs. 3 and 4). Since the slit has been always centered on the central star, the deduced angular width represents the radial extent of each component. Table 2 presents the mean velocity widths and angular widths of the various components, averaged over all PAs where the components have been detected. It should be noted that the widths of the components AA′ to FF′ do not vary significantly with the PA. In the case of components JJ′, the velocity width increases from 10 to 17 km s^{-1} if one proceeds to larger angular distances. We note that the widths of components CC′ quoted in Table 2 are rather uncertain because these components have not been fully resolved at all PAs. The deduced angular width of each component has been marked in Fig. 6 by the separation of the two thick lines following its spatial distribution.

Figure 6 shows that the various components have the appearance of (more or less extended, or closed) "filaments" which show different orientations on the sky, with respect to the radial direction toward the central star. Components AA′, BB′ and DD′ are oriented approximately perpendicular to the radial direction, whereas components FF′ and JJ′ are oriented nearly parallel to the radial direction. Hence, the radial extent of components AA′, BB′ and DD′ quoted in Table 2 can be interpreted as the "diameter" of a filamentary structure, whereas the measured extent of FF′ (Table 2) represents their "length" (not related to their "diameter"). The same is true for components JJ′. As we will show below, components FF′ and JJ′ correspond to the polar condensations and to the bipolar jet-like features, respectively (see Fig. 6d and 6e). Since no long-slit spectrum has been taken perpendicular to the orientation of elongated condensations FF′ and JJ′, their "diameters" can not be deduced directly, but have to be estimated from direct images of NGC 6543. Both the [N II] and [S II] images (BP; Fig. 1) indicate an angular "diameter" (FWHM) of $\leqq 2''$ for each of FF′ and JJ′. By comparing the results in Table 2, one recognizes that all components exhibit surprisingly similar "diameters" and velocity widths. Furthermore, the angular "diameters" and velocity widths are very small compared to the total angular extent of the object ($\approx 40''$, including JJ′) and to the total velocity width of the [N II] emission (≈ 100 km s^{-1}), respectively. From these findings we conclude that the [N II] emission arises in relatively narrow regions of the object.

As already mentioned, components AA′ are detected at each PA (Fig. 6a). We note, however, that component A and D overlap each other between PAs 310° and 340° (Fig. 4). Although component A is definitively present, its radial velocity and spatial position in that interval of PAs are somewhat uncertain. As it can be seen in Fig. 6a, components AA′ trace an ellipse on the plane of the sky. Obviously, the emission from components AA′ is related to the PA 115° Ellipse observed on direct images of NGC 6543 (Fig. 1; see Introduction). The radial velocity varies on the ellipse in a systematic manner. Maximum radial velocity (in absolute value) is observed at the minor axis, minimum radial velocity at the major axis.

Components BB′ (Fig. 6b) are projected upon the sky somewhat farther away from the central star than components AA′. Component B′ is not observed clearly at all PAs, although the isocontours at the expected position (counterpart of B) suggest the presence of an unresolved faint component (see e.g. Fig. 3). The angular distance of BB′ to the central star is approximately constant.

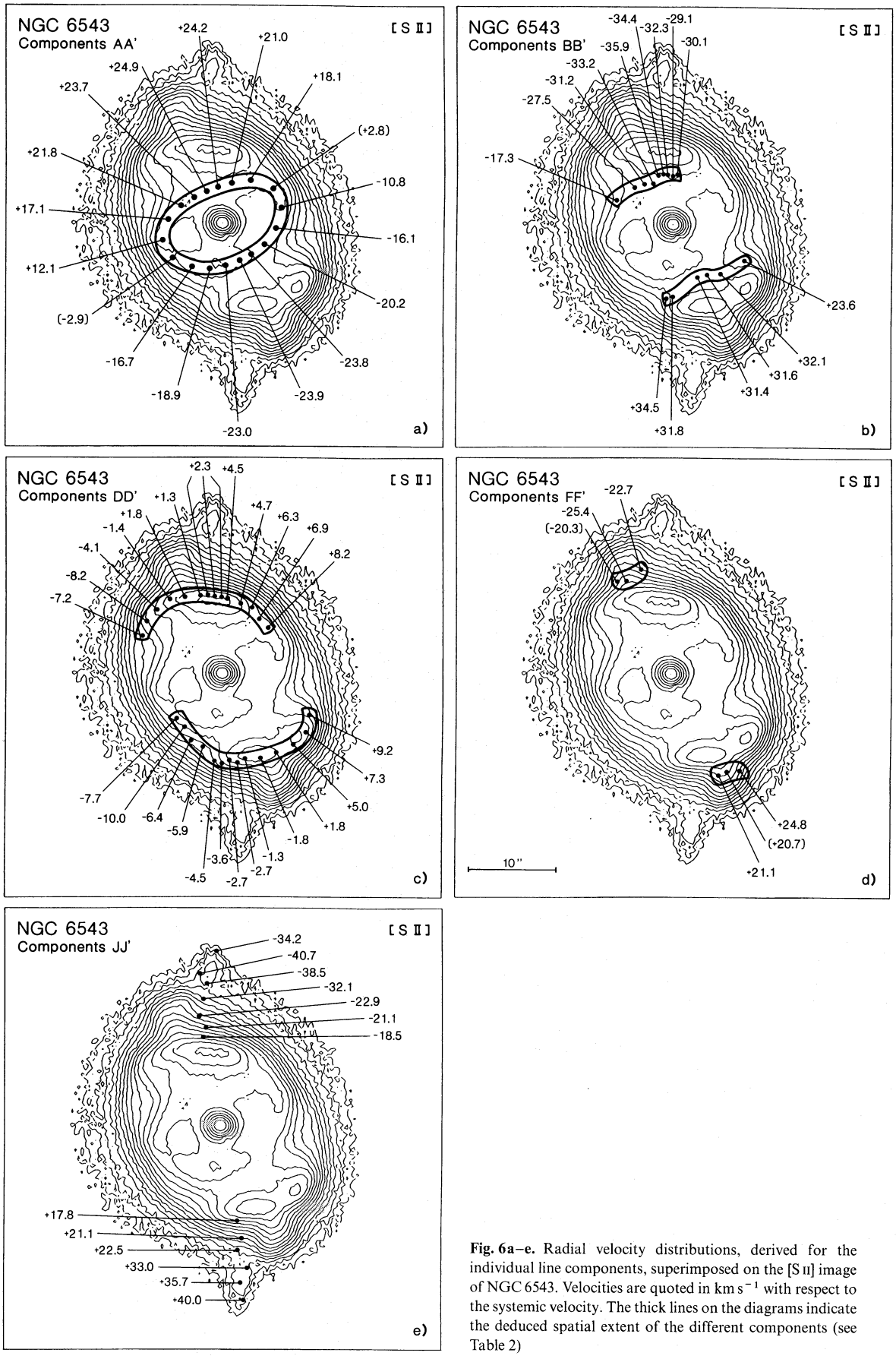

Fig. 6a–e. Radial velocity distributions, derived for the individual line components, superimposed on the [S II] image of NGC 6543. Velocities are quoted in km s^{-1} with respect to the systemic velocity. The thick lines on the diagrams indicate the deduced spatial extent of the different components (see Table 2)

Table 2. Mean velocity width Δv and angular width Δx of the various spectral components detected in the [N II] 6583 line

Component	Δv [a] ($km\,s^{-1}$)	Δx [b] (arcsec)
AA′	12.3	1.6
BB′	13.3	1.6
CC′	16.0	$\leqq 1$
DD′	14.6	1.5
FF′	10.0	2.1
JJ′	10.0	[c]

[a] FWHM corrected for instrumental resolution.
[b] FWHM corrected for seeing.
[c] See Sect. 3.2.

Components DD′ (Fig. 6c) correspond to the prominent "polar caps" (Fig. 1; see Introduction). However, as shown above, the denomination "caps" seems less suitable, since DD′ appear to be a filamentary structure within the elliptical envelope of the nebula (see Fig. 6c). On the other hand, the small radial velocities (relative to the systemic velocity) observed in DD′ suggest that the components move near the plane of the sky (as already pointed out by BP). The variation of the radial velocity and spatial position of DD′ can be recognized in Fig. 6c. As the slit rotates clockwise, the radial velocity (absolute values) of DD′ decreases, changes its sign at PA $\approx 25°$, and increases again. Furthermore, the angular distance of DD′ to the central star increases with increasing PA.

Components FF′ correspond to the strong polar condensations which are extending along the major axis of the elliptical envelope (Fig. 6d). They have been detected only in a small interval of PAs. As already mentioned, components FF′ present a structure that is more elongated along the radial direction than the majority of the other components in the nebula and can be traced from $\approx 11''$ up to $\approx 15''$ (total angular extent at 5% level of the intensity peak). On direct images (Fig. 1), components FF′ appear as slightly curved features. The radial velocity increases slightly along the radial direction (mean velocity gradient $\approx +1.2\,km\,s^{-1}$ per arcsec).

Components JJ′ correspond to the bipolar jet-like features well outside the elliptical envelope. Figure 6e shows the radial velocity field in the jet-like features JJ′. Components JJ′ can be traced on the PV maps from $\approx 10.5''$ up to $\approx 23''$ from the central star. We note that the minimum angular distance is an upper limit because of the presence of strong emission from other components (see Fig. 3). The radial velocity (in absolute value) increases from a minimum of $\approx 18\,km\,s^{-1}$ up to a maximum of $\approx 40\,km\,s^{-1}$ (mean velocity gradient $\approx +2.6\,km\,s^{-1}$ per arcsec), and then decreases to $\approx 34\,km\,s^{-1}$ (mean gradient $\approx -2.3\,km\,s^{-1}$ per arcsec). It should be noted that BP considered components JJ′ and FF′ to be related to each other in the sense that FJ and F′J′ are members of one pair of kinematical components (the "tails"). Our data do not support this interpretation. If J were a prolongation of F, one would expect that the minimum distance, at which J is detected, would coincide with the maximum distance where F is detected. However, J can be traced also at distances smaller than that of F. The same is true for J′ and F′. In addition, JJ′ are (relatively) faint features compared to FF′ which are about 30 times brighter. These results show that FF′ and JJ′ are probably distinct components. The similarity of the radial velocities observed in FF′ and JJ′ at about comparable angular distances from the central star (Fig. 6d and e) is probably due to projection effects.

As already mentioned, an inner elliptical line feature E can be traced on the PV maps at each PA (see Fig. 3b and Fig. 4). At PAs around 25°, only sections of feature E near the minor axis can be recognized, because the other regions are superimposed by the bright components AA′ to DD′. The inner ellipse E is tilted with respect to a vertical line on the PV maps; the amount of tilt depends on the PA. Maximum and minimum tilts of the feature are observed at PA $\approx 25°$ and at PA $\approx 105°$, respectively. Feature E circumscribes an inner region where [N II] and [S II] has not been detected and [O III] and Hα present minimum intensity. On the PV maps of the [N II] emission, the angular diameter of the "empty" inner region varies from $\approx 6''$ (at PA 105°) up to $\approx 12''$ (at PA 25°). The maximum velocity difference observed in feature E occurs at the stellar position. Table 3 lists the maximum velocity differences deduced for the various observed lines.

Components CC′ are detected only between PA 5° and 25°. On the PV maps, they are located near the major axis of the inner ellipse E, suggesting that some relationship exists between components CC′ and E. The radial velocity (absolute values) of CC′ varies between $\approx 12\,km\,s^{-1}$ and $\approx 23\,km\,s^{-1}$ (C is blueshifted).

3.3. Spatial distribution of line intensity ratios

Relative line intensities have been obtained as a function of the spatial position (along the slit) from the CCD (Cassegrain and coudé) spectra, by integrating each emission line in the velocity interval where it is observed. It should be noted that, in case of the Hα emission from the jet-like features, the contribution of the Hα emission from the halo surrounding the object has been taken into account. (The coudé spectra, on which the Hα emission from the jet-like features and that from the halo are spectrally resolved, indicate that the two contributions are of approximately the same amount.)

Figure 7a presents the spatial distributions (along PA 5°) of the [S II] 6716 + 6731 intensity and of the electron density N_e, deduced from the [S II] 6731/6716 ratio for an adopted electron temperature $T_e = 10^4$ °K (Pottasch 1984). It should be noted that, because of the moderate spectral resolution, only components AA′, DD′ and JJ′ can be recognized on the Cassegrain spectra (see Fig. 7a). Figure 7b shows the spatial distribution of the various line ratios deduced from the Cassegrain spectra (PA 5°). In Fig. 7a, b and in the following, [S II] denotes the sum of [S II] 6716 + [S II] 6731, [O I] that of [O I] 6300 + [O I] 6363; [S III] and [N II] refer to [S III] 6310 and [N II] 6583, respectively. In general, the deduced line ratios in the various components agree with those

Table 3. Velocity difference of line splitting at the position of the central star

Emission line	ΔV ($km\,s^{-1}$)
[S II]	41.0
Hα	34.2
[N II]	37.4
[S III]	33.7
He I	31.4
[O III]	32.0

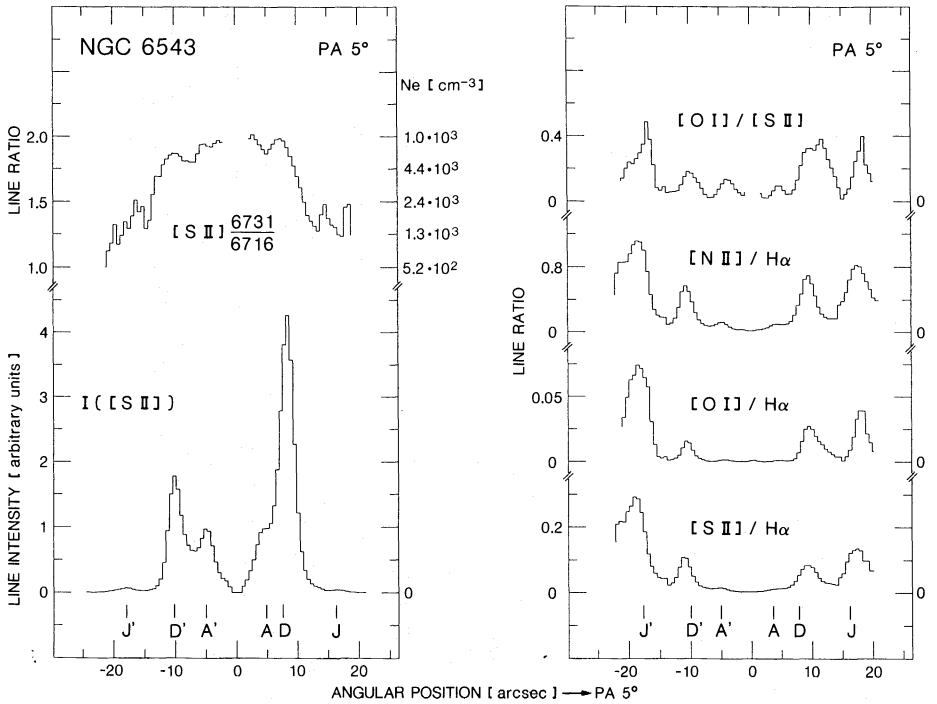

Fig. 7. a Spatial distributions along PA 5° of the [S II] 6716+6731 line strength and of the [S II] 6731/6716 intensity ratio. The corresponding electron density N_e is indicated at the right margin. The identified line components are indicated. **b** Spatial distribution along PA 5° of various line intensity ratios

quoted by BBHO, except for the jet-like features JJ′ where our values are higher.

The electron density is rather high ($\approx 10^4\,cm^{-3}$) for AA′ and DD′, but much lower for JJ′ ($\approx 10^3\,cm^{-3}$). In DD′, the deduced N_e is somewhat lower than the values obtained by Boeshaar et al. (1974). This may be due to internal variations of N_e within each component. (Note that our slit position is slightly different from those used by Boeshaar et al.). The mean value of N_e deduced for the whole nebula is $\approx 6\ 10^3\,cm^{-3}$. Since the [S II] emission of the whole nebula is dominated by that from the bright components AA′ and DD′, presenting higher densities than the mean value, it can be concluded that the density in the fainter components (particularly in the inner elliptical feature E) is significantly lower than $5\ 10^3\,cm^{-3}$.

The line ratios in Fig. 7b provide intersting information about the excitation degree and excitation conditions of the various components. The [O I]/Hα, [S II]/Hα and [N II]/Hα ratios present local maxima at the positions of components AA′, DD′ and JJ′. In DD′ and JJ′, these ratios are high, indicating a low excitation within these components. Moreover, the lowest excitation is observed in the jet-like components JJ′. On the other hand, the deduced values of [O I]/Hα and, particularly, [S II]/Hα and [N II]/Hα in DD′ and JJ′ are much higher than typical values observed in PNs (Barker 1978; Aller & Czyzack 1983), suggesting shock excitation and/or peculiar abundances in DD′ and JJ′ (as already pointed out by BBHO). However, abundance effects should not be present in sulfur (see e.g. Beck et al. 1981) indicating that shock excitation is the more plausible explanation. Shock excitation and/or abundance effects may also exist in FF′, where the [N II]/Hα ratio reaches values of ≈0.65 (deduced from CCD coudé spectra). In the case of AA′, the ratios of [O I]/Hα, [S II]/Hα and [N II]/Hα are rather low, even lower than typical values found in PNs, suggesting that the PA 115° Ellipse represents a structure of rather high excitation. This is confirmed by the fact that the [O III] emission from that ellipse is very strong (see Introduction) and that the [S III]/Hα ratio presents local maxima in AA′. In contrast, the [S III]/Hα ratio exhibits local minima near the positions of the components DD′ and JJ′, as expected from the low excitation degree of these components. The [O I]/[S II] ratio (Fig. 7b) presents a local maximum at the position of each component. In the cases of AA′ and DD′, this effect may be caused by [S II] line quenching due to the high density in these components (see e.g. Mundt et al. 1990). In the case of JJ′, where the density is low, the (relatively) high [O I]/[S II] is probably due to a very low excitation degree within the jet-like features.

4. Discussion

In the following, we will attempt to establish (three-dimensional) spatio-kinematical models in order to explain the observed velocity fields of the various nebular components. For that purpose, we will define three different groups of line components, according to their general properties: 1) the inner elliptical line component E, 2) the line components AA′, BB′, DD′ and FF′, and 3) the jet-like line components JJ′. Each of these groups will be discussed separately.

4.1. Spatio-kinematical model for component E

The fact that line component E has the shape of a closed ellipse that is present on the PV maps at all PAs indicates the existence of an expanding central spheroidal shell in the nebula. Since the tilt of the ellipse varies with the slit PA, the spheroid must be elongated and its major axis be inclined with respect to the plane of the sky. The axis is projected at PA ≈ 25°, where the tilt of the ellipse reaches its maximum. Moreover, the angular extent of feature E on each PV map matches the angular diameter (at the corresponding PA) of the PA 25° Ellipse observed on direct images of NGC 6543 (see Introduction). Obviously, the PA 25° Ellipse is the projected image on the sky of the expanding elongated spheroidal shell that is inferred from the elliptical line feature E on the PV

Table 4. Deduced model parameters for the Inner and Outer Ellipsoids[a]

	Inner Ellipsoid	Outer Ellipsoid
Length of polar axis	0.102 pc	0.153 pc
Length of minor axis	0.051 pc	0.093 pc
Polar expansion velocity	32.8 km s^{-1}	46.1 km s^{-1}
Equatorial expansion velocity	16.4 km s^{-1}	28.0 km s^{-1}
Inclination angle of the polar axis (with respect to the sky)	35°	34°
Position angle of the polar axis	24°	29°
Kinematical age	1520 yr	1625 yr

[a] Distance = 1170 pc.

maps. BP interpreted that PA 25° Ellipse as a tilted ring. However, this interpretation cannot account for the fact that component E is observed as a *closed* elliptical line feature *at all slit PAs*. If the PA 25° Ellipse were a ("two-dimensional") ring, it would be intersected by each slit position at two "points" only, resulting in two symmetric compact components on the PV maps, rather than in a closed ellipse.

In order to explain the kinematics and geometry of component E, we will assume the model of an expanding prolate ellipsoid, whose major (polar) axis is tilted with respect to the sky. We will refer to this as the "Inner Ellipsoid". From the various PV maps, we have obtained about 150 data points, which define the radial velocity field of component E. Components CC′ will be considered as a part of the Inner Ellipsoid (see above). Using a non-linear least-squares fit of the model ellipsoid to the data points, and assuming a distance of 1170 pc (Castor et al. 1981) for NGC 6543, we obtain a set of model parameters (lengths of the major and minor axis, orientation of the polar axis, polar and equatorial expansion velocity, kinematical age) for the Inner Ellipsoid. The results are given in Table 4.

The deduced model parameters permit us to calculate the expected two-dimensional line shape for each PA. Figure 8 shows the predicted line shapes for PA 25° and 105°, superimposed on the corresponding PV maps of the [N II] line. It can be noticed that the model predictions agree reasonably well with the observations. Furthermore, the results suggest that components CC′ are located near the poles of the Inner Ellipsoid and, hence, probably represent bright polar caps.

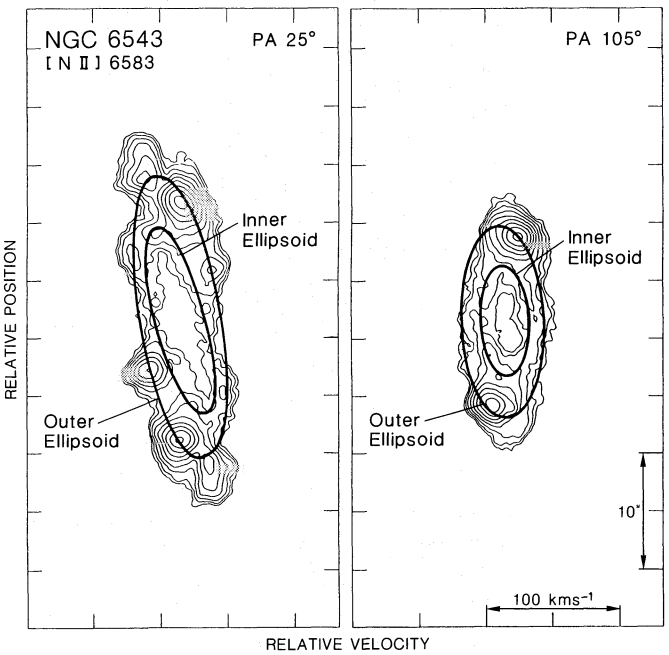

Fig. 8. Elliptical line shapes, at PA 25° and 105°, predicted by the kinematic model using the parameters derived for the Inner and Outer Ellipsoids (Table 4). The schematic lines shapes are superimposed on the PV maps of [N II] at the corresponding PAs

4.2. Spatio-kinematical model for components AA′, BB′, DD′ and FF′

On the PV maps (Fig. 4), the intensity peaks of the components AA′, BB′, DD′ and FF′ can be circumscribed by an outer ellipse (see Sect. 3.1). This fact suggests that these components are located on the "surface" of an expanding shell which is probably ellipsoidal as well. This hypothesis is strongly favored by direct images of NGC 6543 presenting an elliptical envelope which closely surrounds the components. This envelope can be interpreted as the projection of an ellipsoidal structure. We will refer to this ellipsoidal structure as the "Outer Ellipsoid". Both the size and the tilt of the ellipses (traced by components AA′, BB′, DD′ and FF′ on the PV maps) vary with PA and reach their maximum at PA ≈ 25°, indicating that the major axis of the Outer Ellipsoid is oriented at PA ≈ 25°. This orientation is in excellent agreement with that of the polar axis of the elliptical envelope (see Introduction).

If our hypothesis is correct, the velocity fields of AA′, BB′, DD′ and FF′ must fit the velocity field expected from an expanding ellipsoidal shell. In order to test this hypothesis more quantitatively, we will assume that all components are located on the "surface" of a prolate ellipsoidal shell and have (approximately) the same kinematical age. We apply the same fit procedure as used for the Inner Ellipsoid (Sect. 4.1). In this case, the data points are given by the radial velocity fields of components AA′, BB′, DD′ and FF′ (Fig. 6). The model parameters obtained from the fit for the Outer Ellipsoid are listed in Table 4. Figure 8 presents the line shapes predicted by the model superimposed on the PV maps of the [N II] 6583 emission line at PA 25° and 105°, respectively. As it can be seen in Fig. 8, the model accounts rather well for the positions of the components AA′, BB′, DD′ and FF′ on the PV maps. The same is true for other PAs as well. The center of the Outer Ellipsoid coincides with the position of the central star. Moreover, the two components of each pair of symmetric components are located in diametrically opposite regions on the

"surface" of Outer Ellipsoid. Nevertheless, we note some deviations between the model predictions and the observations (see Fig. 8), indicating that the adopted ellipsoidal form is a simplifying approximation.

It has been assumed in the model that all components of the Outer Ellipsoid have approximately the same kinematical age which is the age of the Outer Ellipsoid (Table 4). However, the situation in components FF′ seems to be somewhat different, because these components are somewhat elongated in the radial direction. The inner edge of these components is located on the Outer Ellipsoid and shares its kinematical age. However, the kinematical age deduced for the outer edge is ≈ 600 yr larger. This suggests that the formation of FF′ may have preceded that of the Outer Ellipsoid, although a deceleration of components FF′ can not be ruled out.

Table 4 indicates that the Outer and Inner Ellipsoids present very similar ratios of their axes, similar orientations in space, and kinematical ages. The expansion velocity of the Outer Ellipsoid is higher than that of the Inner Ellipsoid. However, Fig. 8 indicates that most of the region between the inner and outer ellipses is filled up with line emission presenting kinematical and spatial properties intermediate to those of the two ellipses. Hence, the region between the Inner and Outer Ellipsoids must be filled up with ionized material. These results strongly suggest that the Outer and Inner Ellipsoids represent the inner and outer "surface" layers of a single, geometrically "Thick Ellipsoid". The inner layer (Inner Ellipsoid) presents a more uniform brightness distribution than the outer layer (Outer Ellipsoid) which is particularly bright at the positions of the components AA′ to FF′.

In order to study the (three-dimensional) distribution of the individual components AA′, BB′, DD′ and FF′ on the Outer Ellipsoid, we have transformed the cartesian coordinates (x, y, z) (deduced from the PV maps) into polar coordinates (r, θ, ϕ) in the reference frame of the model ellipsoid (described by the model parameters of Table 4). Table 5 presents the intervals of the spatial distribution of the various components in polar coordinates. From Table 5 the following results are deduced:

(1) AA′ have been detected at all longitude angles ($0° \leqq \phi \leqq 360°$), but only in a narrow equatorial zone ($-5° \leqq \theta \leqq 5°$) of the Outer Ellipsoid. This implies that AA′ can be interpreted as an equatorial ring. The deduced expansion velocity of the equatorial ring is $\approx 28\,\mathrm{km\,s^{-1}}$.

Table 5. Spatial distribution of components AA′, BB′, DD′ and FF′ in the reference system of the Outer Ellipsoid

Component	r [a] (pc)	θ [b] (degree)	ϕ [c] (degree)
AA′	0.046	−5–+5	0–360
B	0.065	+65	40–150
B′	0.065	−65	220–330
D	0.062–0.046	+60–0	190–340
D′	0.062–0.046	−60–0	10–160
F	0.076	$\geqq +80$	–
F′	0.076	$\leqq -80$	–

[a] Radius vector for distance of 1170 pc.
[b] Latitude angle.
[c] Longitude angle measured from west towards east clockwise.

(2) FF′ are confined to a narrow zone at each pole of the Outer Ellipsoid ($|\theta| \geqq 80°$). The deduced expansion velocity is $\approx 46\,\mathrm{km\,s^{-1}}$ in the direction of the pole. The polar axis of the Outer Ellipsoid is tilted such that F approaches towards the observer and F′ recedes.

(3) In the case of BB′, the latitude angle θ presents a constant value (Table 5). This implies that BB′ form sections of a "latitude circle" on the Outer Ellipsoid, which show a constant expansion velocity ($\approx 40\,\mathrm{km\,s^{-1}}$).

(4) In the case of DD′, we notice that the longitude angle and the latitude angle vary at the same time. In particular, the latitude angle $|\theta|$ (absolute value) decreases monotonously from $\approx 60°$ (at $\phi \approx 190°$ for D, $\phi \approx 10°$ for D′) to $\approx 0°$ (at $\phi \approx 340°$ for D, $\phi \approx 160$ for D′). Hence, these components form two oblique arcs on the Outer Ellipsoid. The expansion velocity in DD′ decreases from $\approx 38\,\mathrm{km\,s^{-1}}$ ($|\theta| \approx 60°$) to $\approx 28\,\mathrm{km\,s^{-1}}$ (equator).

4.3. Spatio-kinematical model for the jet-like features JJ′

The elongated shape and the kinematics of components JJ′ suggest that these features represent a collimated bipolar outflow system with an axis that is inclined with respect to the plane of the sky and projected upon the sky at PA $\sim 5°$. The space orientation of the JJ′ flow axis is not known. It is not related to that of the polar axes of the Inner and Outer Ellipsoid, because of the large difference in the PAs (see Table 4).

In the following, we will use the model of a precessing jet to describe the outflow characteristics of components JJ′. Precession has been already considered by BP to explain characteristics of these features. We will assume that the (amount of the) outflow velocity V_e of the jet material is constant and that the observed S-type curvature and radial velocity variation (see Fig. 6e) are due to a systematic change of the flow direction. The path of a precessing jet can be circumscribed by a narrow cone with its apex at the central star. The (half) aperture angle Φ of the cone corresponds to the precession angle. The inclination angle of the cone axis (with respect to the plane of the sky) will be designated by Θ. Maximum (minimum) radial velocities v_{max} (v_{min}) are expected to occur on the far (near) side of the cone, close to the projected cone axis. In this case, the actual inclination of the outflow direction is $\Theta + \Phi$ and $\Theta - \Phi$, respectively. Adopting the model of biconical outflow of Solf & Carsenty (1982) one obtains

$$\mathrm{tg}\,\Theta = \frac{v_{max} + v_{min}}{v_{max} - v_{min}}\,\mathrm{tg}\,\Phi, \tag{1}$$

$$V_e = \left[\left(\frac{v_{max} + v_{min}}{2\cos\Phi}\right)^2 + \left(\frac{v_{max} - v_{min}}{2\sin\Phi}\right)^2\right]^{1/2}. \tag{2}$$

The S-type morphology of components JJ′ (Fig. 6e) suggests that the projected cone angle is of the order of 5°–10°. We will adopt these values as a reasonable approximation of the true aperture angle 2Φ. Furthermore, we will adopt the maximum and minimum values of the radial velocity observed within JJ′ (see Sect. 3.2) as approximation for v_{max} and v_{min}, respectively. For $2\Phi = 5°$ (10°), we obtain $\Theta \approx 6.5°$ (13°) and $V_e = 255\,\mathrm{km\,s^{-1}}$ ($130\,\mathrm{km\,s^{-1}}$). The kinematical age of the jet-like features increases outwards, ranging from ≈ 230 yr (450 yr) to ≈ 470 yr (940 yr).

The deduced high expansion velocity, and the length-to-diameter ratio of >6 (see Sect. 3.2) suggest that the jet-like features JJ′ represent high collimated bipolar jet-like ejections from the central star. These ejections have probably occurred later than the formation of the Thick Ellipsoid. It is noteworthy that

both the PA and inclination angle of JJ′ differ by $\approx 20°$ from those of the major axis of the Thick Ellipsoid.

We have assumed above that the amount of V_e is constant all along the jet-like features. However, this may not be necessarily true. We note that the slight decrease of the radial velocity at the outer tips of the features (Fig. 6e) may also be explained if the jet-like features have been somewhat decelerated. This is partially supported by the large velocity width observed at increasing angular distances from the star. If so, interaction of the front-ends of the jet-like features with material in the halo surrounding the object might be the cause of the deceleration.

4.4. *Excitation conditions*

The Inner Ellipsoid is a high-excitation structure (see Introduction), although low-excitation emissions ([S II], [N II]) from the Inner Ellipsoid have been detected, too. Table 3 indicates a correlation between the ionization potential of the emission lines and the velocity difference of the line splitting, suggesting a stratification effect in the Inner Ellipsoid (Wilson 1950). Hence, it is expected that the high-excitation emissions (e.g. [O III]) originate in regions closer to the star than those where the low-excitation emissions (e.g. [N II]) originate. This further supports our interpretation that the Inner Ellipsoid represents the inner shell of the Thick Ellipsoid in which the excitation degree decreases outwards.

As already mentioned, the observed [S II]/Hα ratio indicates that shock excitation may be present in DD′ and JJ′. Moreover, the high expansion velocity deduced for the jet-like features JJ′ is compatible with shock excitation. On the other hand, the material of the nebula is subject to photoionization by the central star. It is unknown how the two mechanism (shocks and photoionization) contribute to the intensities of the different emission lines from NGC 6543. Hence, shock velocities in DD′ and JJ′ estimated by comparing the observed line ratios with those predicted from theoretical pure shock models, may be unreliable. The situation is even more complex, since, *in addition* to shock excitation, abundance effects may be important, too. It has been reported that nitrogen is overabundant in NGC 6543 (Pottasch 1984; Manchado & Pottasch 1989), which may explain the unusually strong [N II] emissions from DD′ and JJ′. Shock excitation *and* overabundance of N probably exist in FF′ (see Sect. 3.3).

The situation is probably different in the equatorial ring represented by AA′. This ring is a (relatively) high-excitation structure (see Sect. 3.3). Evidence for shock excitation in AA′ has not been found. On the other hand, it can not be ruled out that the line ratios observed in AA′ reflect a chemical composition which is different from that in the other components on the outer ellipsoid. If so, the origin of the equatorial ring may be different from that of the other components.

4.5. *Ionized masses of the components*

Crude estimates for the ionized mass can be made in the cases of components AA′, DD′ and JJ′ where the electron density has been deduced. We will assume a circular cross-section for each component (Table 2). An abundance of helium by number of 0.1, and a filling factor of 0.6 are assumed throughout. The ionized masses are: $M(\mathrm{AA}') \approx 4\ 10^{-3} M_\odot$, $M(\mathrm{DD}') \approx 3\ 10^{-3} M_\odot$, and $M(\mathrm{JJ}') \approx 2.5\ 10^{-4} M_\odot$. The results show that the mass of the jet-like features is smaller by an order of magnitude than that in the other components.

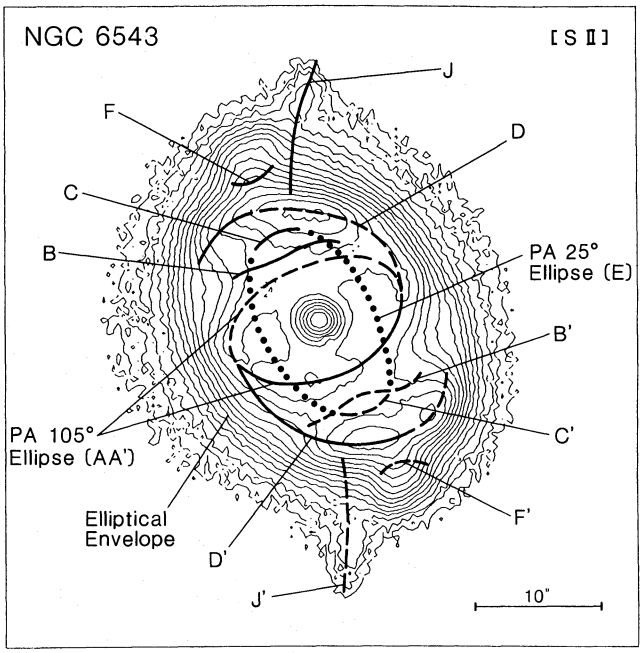

Fig. 9. Schematic representation of the various components in NGC 6543, superimposed on the [S II] image of the nebula. Component E is represented by dotted lines; all other components by continuous or dashed thick lines. Continuous thick lines indicate redshifted features, dashed thick lines blue-shifted ones. Component E (the PA 25° Ellipse) is interpreted as a prolate ellipsoidal structure (Inner Ellipsoid); components CC′ represent bright polar caps of the Inner Ellipsoid. Component AA′ (the PA 115° Ellipse) is interpreted as an equatorial ring. Components BB′, DD′ and FF′ are point-symmetric filamentary structures. Components FF′ represent polar condensations. Components AA′, BB′, DD′ and FF′ are located on the Outer Ellipsoid that corresponds to the elliptical envelope (see text). Components JJ′ are bipolar jet-like features extending beyond the elliptical envelope and not related kinematically to the Outer Ellipsoid

4.6. *Possible formation processes of the various nebular components*

Figure 9 shows a schematic representation of the various components identified in NGC 6543, superimposed on the [S II] image of the nebula. In the following, we will attempt to explain how the various nebular components may have been formed.

According to the ISW model, axial-symmetric (bipolar) PNs result from the interaction of the "fast" wind from the central star with an anisotropic envelope ("slow" wind) of the progenitor red giant (e.g. Balick 1987, Kahn 1989). Soker & Livio (1989) showed that ISW model calculations can reproduce elliptical and bipolar shapes observed in PNs, assuming that a density contrast exists in the slow wind between the equatorial and polar directions. The Thick Ellipsoid in NGC 6543 (see Sect. 4.2) could be explained by the ISW model. Nevertheless, it is somehow surprising that an anisotropic slow wind in NGC 6543 must be postulated, because the halo surrounding the bright nebula, which is probably related to the slow wind (Hippelein et al. 1985), is circular. This could be explained if the hypothesized anisotropic mass loss from the central star of NGC 6543 is a (relatively) recent phenomenon, compared to an earlier phase of spherical mass loss (see below). We further note that the role of the fast wind in NGC 6543 does not seem to be restricted to the formation of the Thick Ellipsoid. Middlemass et al. (1989) and Meaburn et al. (1991) found evidence that material in the halo is shocked by the stellar wind.

The required density contrast in the slow wind could be generated by a binary star in the center of the PN (see Livio & Soker 1988 and Soker & Livio 1989). There is some evidence for the existence of a binary star in NGC 6543, although the various observations present various inconsistencies (see BP and references therein; Bentley 1989). We will assume that the binary consists of a mass lossing red giant and a compact companion. If the system initially is a wide binary, the presence of the companion will not critically affect the ejection from the red giant (slow wind), and the resulting shell geometry will be spherical. The remnant of this spherical shell can be identified with the halo surrounding the object. If mass transfer occurs in the binary, the separation between the stars will be reduced (Livio et al. 1979), and the stars can eventually evolve in a common envelope phase. In this phase, the slow wind will be mainly ejected in the orbital plane of the binary (Livio & Soker 1988; Soker & Livio 1989). Moreover, under several conditions (see Morris 1987), it is possible that a circumbinary disk is formed. Therefore, the density distribution around the stars is anisotropic. As soon as the red giant evolves beyond the AGB stage and its fast wind starts, the resulting expanding ionized shell will be ellipsoidal or bipolar (see above). According to this model, the equatorial ring AA′ is probably related to material swept up in the equatorial plane.

Components BB′, DD′ and the jet-like features JJ′ deviate considerably from the axial symmetry expected from the ISW model. An interesting question is, which process may be responsible for their formation. Breitschwerdt & Kahn (1990) proposed that filaments and condensations in PNs are due to instabilities in the shell. However, in the case of BB′ and DD′, it is difficult to understand how instabilities can result in the formation of highly symmetric (space and velocity) pairs of filaments. As already mentioned (see Introduction), the ISW model presents some difficulties in explaining polar condensations in bipolar PNs. In particular, recent results by Socker (1990) and Icke et al. (1991) show that polar condensations do not result from a focusing of the fast wind by an elongated inner shock (see Balick et all 1987b; Icke 1989). Therefore, these authors suggest that polar condensations may be the result of direct ejections from the central star. The results obtained for the polar condensations FF′ seem to point into the same direction. Our analysis of the kinematics suggests that the formation of FF′ has preceded that of the Thick Ellipsoid. As already mentioned (Sect. 4.3), the formation of the bipolar jet-like features JJ′ probably requires a direct ejection from the central star.

The high symmetry observed in BB′, DD′ and FF′ suggests that these condensations are the result of highly collimated bipolar mass ejections from the central star. Since the components are curved filaments, an additional mechanism must be active during the ejection process, which causes the bipolar flow axis to change its orientation. This could be the result of precession. If so, the orientation and curvature of the components will depend on the precession angle and on the angular velocity of the precession. For (relatively) high precession velocities (compared to the ejection velocity) and precession angles of, say, $> 20°$, the components will be oriented nearly perpendicular to the (radial) outflow direction (e.g. BB′ and DD′), whereas for small precession angles the components will be oriented along the radial direction (e.g. FF′ and jet-like features). We have shown above that BB′ and DD′ are structures located on the "surface" of the Outer Ellipsoid. This implies that their ejection must have occurred in a time interval which is much shorter than their kinematical age of ≈ 1600 yr.

If the precession hypothesis is correct, each component is located on the "surface" of a conus which intersects the ellipsoid, and whose apex coincides with the central star. Hence the deduced three-dimensional distribution of each component contains some information about the precession geometry. In the case of BB′, the latitude angle θ has a constant value of $\approx 65°$ (Table 5), suggesting that the precession axis coincides with the polar axis of the Thick Ellipsoid, and that the precession angle is $\approx 25°$.

In the case of the polar features FF′, precession is also suggested by the slight variation of the radial velocity along FF′ and by the curvature on direct images. As in these case of BB′, the precession axis coincides with the polar axis of the Thick Ellipsoid. However, the direct images and the spectra suggest a precession angle of $\approx 10°$ for FF′.

In the case of the jet-like features, *both their spatial and kinematical properties* are compatible with the idea that the jet-like features have been ejected along a precessing axis (BP; Sect. 4.3). The precession axis is oriented at PA $\approx 6°$ and the precession angle is $\leqq 10°$ (see Sect. 4.3). Comparison of the results obtained from BB′, FF′ and the jet-like features JJ′ shows that the precession axis and precessing angle have varied with time.

In the case of components DD′, the precession model presents difficulties for explaining the deduced spatial distribution because of the large variation of the latitude angle θ (Table 5). If DD′ are the result of precession, the precession axis must be oriented such that the precession angle is constant. This would imply that the orientation of the precession axis for DD′ is significantly different from that deduced for BB′, FF′ and the jet-like features. We cannot rule out this possibility because a variation of the orientation of the precession axis is indicated by the other components as well. In any case, components DD′ present very peculiar properties and a satisfactory explanation for their formation has not been found.

All these findings suggest the existence of a precessing agent in the system, which, in addition, causes high collimation of the mass ejections. This collimation is much higher than that predicted by the ISW model (see Socker 1990 and Icke et al. 1991). Morris (1987) proposed a binary model for the creation of bipolar circumstellar outflows. The collimating agent is an accretion disk around the compact companion. This disk may be the result of increasing mass loss from the red giant star at the end of AGB and the expected small separation between the stars. A fast wind from the companion, caused by mass accretion through a disk, will be intrisically bipolar and highly collimated, probably similar to the wind from young stars (see e.g. Shu et al. 1991; Mundt et al. 1990). It seems that Morris' model is a promising possibility for explaining the formation of the filamentary components in NGC 6543. The resulting ejections from the inner parts of the accretion disk will generate highly collimated bipolar structures. However, if the plane of the accretion disk does not coincide with the orbital plane, the disk is forced to precess, resulting in a precessing axis of the bipolar ejection. In this case, the collimated ejecta (located on the surface of a conus) will appear on direct images as curved filamentary structures. The separation between the stars decreases with time, and the size of the accretion disk may vary due to a change of the mass accretion rate. Hence, variations of some precessing parameters may also be expected (see e.g. Iping & Petterson 1990). This scenario could explain the variations of the precession axis and precession angle with time, as indicated by the properties of components BB′, FF′ and JJ′.

5. Conclusions

(1) The velocity field of NGC 6543 derived from high resolution long-slit spectra shows the existence of two concentric ellipsoidal

shells in the nebula. The two shells likely represent the inner and outer "surface layers" of a geometrically "Thick Ellipsoid" which constitutes the basic structure of NGC 6543. The equatorial zone of the Thick Ellipsoid is characterized by a bright ring.

(2) The equatorial expansion velocity of the Thick Ellipsoid increases from ≈ 16 up to $\approx 28\,\mathrm{km\,s^{-1}}$, at the inner and outer shell, respectively. The polar expansion velocities are larger by a factor of ≈ 1.8 than the equatorial expansion velocities.

(3) Four pairs of narrow, filamentary components have been identified in the nebula, including the previously known bipolar jet-like features. The two components of each pair present a high point-symmetry (in space and velocity) with respect to the center of the object.

(4) Three of the pairs of point-symmetric components are embedded in the outer shell of the Thick Ellipsoid. The two components of each pair are located on diametrically opposite regions of the outer shell and participate in its expansion.

(5) The jet-like features (the fourth pair) are probably not related to the Thick Ellipsoid. They seem to be younger and to move at higher velocities compared to the other components.

(6) Shock excitation probably occurs in some of the filamentary components, including the jet-like features.

(7) The spatial and kinematical attributes of the filamentary components suggest that they are the result of highly collimated, bipolar ejections from the central object of NGC 6543. A detailed analysis of *both* the spatial and kinematical properties of the various components suggests that the bipolar ejection source is precessing. A comparison of the precession parameters deduced from the various components shows that the precession axis and the precession angle must have changed with time.

(8) The formation of the complex PN NGC 6543 can qualitatively be explained if the central object is a mass-exchanging binary. The Thick Ellipsoid probably results from the interaction of an energetic stellar wind from the evolved primary with an anisotropic common envelope of the binary. The filamentary components may be attributed to highly collimated, bipolar mass ejections from a precessing accretion disk around the companion. Temporal changes in the separation of the binary components and in the mass accretion rate may cause changes in the size and tilt of the accretion disk and, hence, may lead to temporal variations of the precession parameters of the bipolar ejection source.

Acknowledgements. We are indebted to the staff on the Calar Alto Observatory for assistance during the observations. We thank Dr. U. Hopp for providing the CCD image of NGC 6543. L.F.M. is grateful to Professor H. Elsässer for his stay at the Max-Planck-Institut für Astronomie.

References

Aller L. H., Czyzak S. J., 1983, ApJS 51, 216
Balick B., 1987, AJ 94, 671
Balick B., Bignell C. R., Hjellming R. M., Owen R., 1987a, AJ 94, 948 (BBHO)
Balick B., Preston H. L., 1987, AJ 94, 958 (BP)
Balick B., Preston H. L., Icke V., 1987b, AJ 94, 1641
Barker T., 1978, ApJ 219, 914
Beck S. C., Lacy J. H., Townes C. H., Aller L. H., Geballe T. R., Baas F., 1981, ApJ 249, 592
Bentley A. F., 1989, in: Planetary Nebulae, IAU Symp. No. 131, ed. S. Torres-Peimbert, Kluwer, Dordrecht, p. 312
Bignell R. C., 1983, in: Planetary Nebulae, IAU Symp. 103, ed. Flower, Reidel, Dordrecht, p. 69
Boeshaar G., Czyzak S. J., Aller L. H., 1974, ApJS 28, 335
Breitschwerdt D., Kahn F. D., 1990, MNRAS 244, 521
Castor J. I., Lutz J. H., Seaton M. J., 1981, MNRAS 194, 547
Gieseking F., Becker I., Solf J., 1985, ApJ 295, L 17
Hippelein H. H., Bässgen M., Grewing M., 1985, A&A 152, 213
Icke V., 1989, A&A 202, 177
Icke V., Balick B., Frank A., 1991 (preprint)
Iping R. C., Petterson J. A., 1990, A&A 239, 221
Kahn F. D., 1989, in: Planetary Nebulae, IAU Symp. NO. 131, ed. S. Torres-Peimbert, Kluwer, Dordrecht, p. 411
Kwok S., 1989, in: Planetary Nebulae, IAU Symp. No. 131, ed. S. Torres-Peimbert, Kluwer, Dordrecht, p. 401
Livio M., Salzman J., Shaviv G., 1979, MNRAS 188, 1
Livio M., Soker N., 1988, ApJ 329, 764
Manchado A., Pottasch S. R., 1989, A&A 222, 219
Meaburn J., Nicholson R., Bryce M., Dyson J. E., Walsh J. R., 1991, MNRAS 252, 535
Middlemass D., Glegg R. E. S., Walsh J. R., 1988, MNRAS 239, 1
Millikan A. G., 1974, AJ 79, 1259
Miranda L. F., Solf J., 1990, Ap&SS 171, 227
Morris M., 1987, PASP 99, 115
Münch G., 1968, in: Planetary Nebulae, IAU Symp. No. 34, eds. D. C. Osterbrock & C. R. O'Dell, p. 259
Mundt R., Ray T. P., Bührke T., Raga A. C., Solf J., 1990, A&A 232, 37
Phillips J. P., Ray N. K., Worswick S. P., 1979, A&A 61, 695
Pottasch S. R., 1984, Planetary Nebulae, Reidel, Dordrecht
Schneider S. E., Terzian Y., Purgathofer A., Perinotto M., 1983, ApJS 52, 399
Shu F. H., Ruden S. P., Lada C. J., Lizano S., 1991, ApJ 370, L 31
Soker N., 1990, AJ 99, 1869
Soker N., Livio M., 1989, ApJ 339, 268
Solf J., Carsenty U., 1982, A&A 113, 142
Solf J., Miranda L. F., 1992 (in preparation)
Wilson O. C., 1950, ApJ 111, 279